



Characterizing unforced decadal climate variability in global climate model large ensembles

Bin Yao^{1,2} · Yangyang Xu³ · Andrew E. Dessler³ · Chao Liu⁴

Received: 25 January 2021 / Accepted: 20 July 2021

© The Author(s), under exclusive licence to Springer-Verlag GmbH Germany, part of Springer Nature 2021

Abstract

This paper compiles indices for the El Niño—Southern Oscillation (ENSO) and seven unforced decadal-to-multidecadal climate modes (Interdecadal Pacific Oscillation (IPO), Tripole Pacific Index (TPI), Pacific Decadal Oscillation focused over North Pacific (PDO) and South Pacific (SPDO), North Atlantic Multidecadal Oscillation (AMO), South Atlantic Multidecadal Oscillation (SAMO), and Indian Ocean basin (IOB)) in a 100-member ensemble of the Max Planck Institute Earth System Model (MPI-ESM1.1) and a 35-member ensemble of Community Earth System Model (CESM1). Comparison among various detrending approaches indicates that the best approach to remove the unforced component is by subtracting the ensemble average temperature at each grid point from the original model output. Similar characteristics are investigated in the indices of both MPI-ESM1.1 and CESM1 ensemble models. The results further indicate no statistically significant lead-lag correlations between the unforced multidecadal climate modes originating from North Pacific (e.g., PDO) and North Atlantic (e.g., AMO), suggesting that a high correlation found in previous observational studies may be due to biased detrending approaches.

Keywords Global climate models · Unforced decadal-to-multidecadal climate variability · Atlantic multidecadal oscillation · Pacific decadal oscillation

1 Introduction

Unforced decadal climate variability significantly modulates the rate of climate change at both global and regional scales and can lead to phenomena such as the so-called “hiatus”, a global warming slowdown in the early twenty-first century. Because of the difficulty of separating forced and unforced signal from climate record, the underlying mechanisms governing decadal variability are still under intense debate (Frankignoul and Hasselmann 1977; Knight et al.

2005; Clement et al. 2015). Numerous studies suggest that unforced ocean–atmosphere interactions originating from the Pacific, Atlantic, and Indian Ocean are major drivers of interdecadal climate variability (Delworth et al. 2007; Dong et al. 2016; Meehl et al. 2016; Dong and McPhade 2017a), which can then explain considerable proportions of recent global and hemispheric climate changes (Mantua and Hare 2002; Deser et al. 2012; Si and Hu 2017).

Modes of Pacific decadal variability can be depicted by the Interdecadal Pacific Oscillation (IPO, Power et al. 1999) and the Pacific Decadal Oscillation (PDO, Mantua et al. 1997; Zhang et al. 1997; Mantua and Hare 2002). Both the IPO and PDO are based on empirical orthogonal function (EOF) analysis that extracts information from detrended long-term changes of sea surface temperature (SST). The IPO characterizes the unforced climate variability in the entire Pacific, whereas the PDO characterizes variability in the North Pacific. Similar to the IPO, a non-EOF based metric called the Tripole Pacific Index (TPI, Henley et al. 2015) also characterizes climate variability in the entire Pacific, but is computed using simple differences of regional-average SST. Generally, the IPO, PDO, and TPI are highly correlated in time (Henley et al. 2015; Newman et al. 2016), so they

✉ Chao Liu
chao_liu@nuist.edu.cn

¹ Key Laboratory of Transportation Meteorology, CMA, Nanjing, China

² Nanjing Joint Institute for Atmospheric Sciences, Nanjing, China

³ Department of Atmospheric Sciences, Texas A&M University, College Station, TX, USA

⁴ Collaborative Innovation Center on Forecast and Evaluation of Meteorological Disasters, School of Atmospheric Physics, Nanjing University of Information Science and Technology, Nanjing, China

are often used interchangeably in regional climate impact studies. For example, streamflow and flooding in Australia (Micevski et al. 2006), drought in China (Qian and Zhou 2014), and precipitation in North America (Dai 2013) are shown to be highly correlated to these Pacific-related decadal variabilities. It has also been suggested that Pacific decadal variability has a significant impact on the global warming “hiatus” (Meehl et al. 2013; England et al. 2014; Dong and McPhaden 2017b) and on the observed expansion of Antarctic sea ice in the early of this century (Meehl et al. 2016).

The Atlantic Multidecadal Oscillation (AMO, Schlesinger and Ramankutty 1994; Kerr 2000; Enfield et al. 2001) is traditionally defined as the averaged detrended SST in the North Atlantic Ocean. Recent studies on the AMO variability mainly focused on subpolar North Atlantic region, and found the tropical Atlantic variability is less multidecadal and well correlated with the AMO indices (O’Reilly et al. 2016; Zhang 2017; Kim et al. 2018; Zhang et al. 2019). The AMO has demonstrated not only influence the climate on North America and Europe (Enfield et al. 2001), but also has broader hemispheric effects, for example, on the North African monsoons and the summer rainfall in East Asia and India (Lu et al. 2006; Zhang and Delworth 2006). Moreover, the AMO plays a key role in passing the current climate model bias to the future rainfall projection uncertainties in the Mediterranean climate regions (Dong et al. 2021).

The AMO and PDO/IPO are important sources of low-frequency climate variability in Asia–Pacific region and Northern Hemisphere mid-latitudes (McGregor et al. 2014; Cai et al. 2019). It is found that the internal variability, such as the PDO, may contribute as large as 80% of the decadal variation of East Asia summer monsoon, and external variability only explains ~20% (Zhou et al. 2013; Song et al. 2014). Moreover, the relationship between East Asia summer monsoon and the El Niño—Southern Oscillation (ENSO) variability could be modulated by the PDO (Song and Zhou 2015). It has also been indicated that the AMO-related Atlantic SSTs influence the changes in Walker circulation in the tropical Pacific regions, which modifies the ENSO signals on both annual and multidecadal timescales (Levine et al. 2017).

Although the AMO is centered in North Atlantic Ocean, the PDO component is partly connected to it. Si and Ding (2016) indicated that the AMO plays an important role in altering the PDO through the atmospheric teleconnection, resulting in different PDO patterns between the 1960s and 2010s. Summer East Asian monsoon rainfall anomalies are effectively influenced by the AMO and PDO/IPO modes. The combination of negative IPO and positive AMO was also shown to enhance the recent East Asia jet shift more significantly than the individual factor alone (Huang et al. 2019). However, the relationship between the AMO and

PDO/IPO is still in debate and the temporal correlation of them is a subject we will study in detail in this paper.

Another important climate index, termed the decadal Indian Ocean basin (IOB, Yang et al. 2007), is the first mode of SST variability in the Indian Ocean, and is an important mode for the inter-annual variation of East Asian summer monsoon and rainfall (Song and Zhou 2014a; 2014b). The response to ENSO-included surface heat flux anomalies (Klein et al. 1999) and the tropospheric temperature (Chiang and Lintner 2005) mechanisms are used to explain the formation of IOB, and the air-sea atmospheric interactions shape the spatiotemporal structures (Xie et al. 2010). Because of close interactions between the tropical Indian Ocean and Pacific Ocean, Dong et al. (2016; 2017a) suggested that the evolution of the IOB is strongly influenced by SST in tropical eastern Pacific Ocean, especially the IPO. The IOB also features a slowdown in recent global air temperature warming, and the anthropogenic forcing is considered as the principal cause for the correlation change of the IOB and IPO from around 1985 (Dong et al. 2017a).

The main objective of this study is to characterize indices for the decadal to multidecadal modes of variability in two large ensembles of state-of-art Earth system models. The compiled climate indices and the codes used to derive them can be downloaded at https://github.com/carrolyb/climate_index. Separating the unforced variability from the forced response in the climate record is a critical but unsolved problem in climate research (Wild et al. 2013). Therefore, we will discuss various detrending approaches for separating the unforced climate variability from the climate change response externally forced by anthropogenic activities. Lastly, the simulated lead-lag relationships between those climate modes are also analyzed.

2 Methods

2.1 Model simulations

This study examines interdecadal climate variability using monthly mean values from a 100-member ensemble performed with the Max Planck Institute Earth System Model (MPI-ESM1.1). This “grand” ensemble is discussed in detail in Maher et al. (2019). The model runs cover 1850–2020, and this study uses surface temperature fields archived at a resolution of $1.875^\circ \times 1.875^\circ$. For 1850–2005, all ensemble members are driven by the same historical evolution of natural and anthropogenic forcing, but the initial conditions branch from different states sampled from a 2000-year control simulation. Years 2006 to 2020 are extensions of the historical runs forced by the emission scenarios of Representative Concentration Pathway 8.5 (RCP8.5).

Moreover, the widely studied 35-member large ensemble simulations between 1920 and 2020 in the Community Earth System Model, version 1 (CESM1; Kay et al. 2015) are used. The simulation is performed by CESM1 (Hurrell et al. 2013) and its capability is evaluated in Meehl et al. (2013). The horizontal resolution of the component is at the nominal 1° . Similar to MPI-ESM1.1, all CESM1 ensemble members are driven by the same historical forcing from 1920 to 2005 and RCP8.5 forcing from 2006 to 2020. The only differences among the members are a small round-off level perturbation in the atmospheric temperature on 1 January 1920.

2.2 Observational dataset

The observational dataset used here is from the NASA Goddard Institute for Space Studies (GISS) Surface Temperature v4 (GISTEMP, Lenssen et al. 2019). The ocean temperature products within GISTEMP are based on the NOAA Extended Reconstructed SST (ERSST) (Lenssen et al. 2019) and thus unforced climate variability computed from GISTEMP and ERSST are highly consistent. The GISTEMP dataset is a monthly mean time series at a $2^\circ \times 2^\circ$ horizontal resolution from 1880 to present. Missing values are mainly in polar regions, southern Africa, and some Southern Ocean regions during of the nineteenth century. However, this issue has little effect on the present study, because the indices are mostly computed using SST between 60°S and 60°N .

2.3 Definition of climate modes

Definitions of the unforced climate modes calculated in the study include the following:

- ENSO is calculated as the monthly detrended SST anomalies averaged in the Niño 3.4 region (5°S – 5°N , 170°W – 120°W). The time series is then smoothed with a 5-month rolling mean.
- AMO and SAMO indices are defined as the average of detrended SST in the subpolar North Atlantic (40°N – 60°N , 0° – 80°W) and South Atlantic (60°S – 0° , 60°W – 40°E), respectively.
- TPI is the detrended SST differences between the equatorial Pacific (10°S – 10°N , 170°E – 90°W) and the average of the northwest (25°N – 45°N , 140°E – 145°W) and southwest Pacific (50°S – 15°S , 150°E – 160°W) (Henley et al. 2015).
- IPO, PDO, SPDO and IOB are defined as the time series of the first EOF mode of detrended SST in the entire (60°S – 60°N , 110°E – 70°W), North (0° – 60°N , 110°E – 100°W), and South (60°S – 0° , 110°E – 70°W) Pacific, and the Indian Ocean (30°S – 30°N , 40°E – 120°E), respectively.

Moreover, we also compute the average surface temperature in Northern Hemisphere (0° – 60°N), Southern Hemisphere (60°S – 0°), and near-globally (60°S – 60°N , excluding the high-latitudes) (denoted as “NH”, “SH”, and “GL”, respectively) for the comparison and synthesis in the study.

To emphasize the multidecadal time scale, unforced climate modes other than the ENSO are also smoothed by a low-pass symmetric filter with 13 weights and a half-amplitude point at an appropriately 12-year period (Trenberth et al. 2007), after the EOF or spatial-average analysis. We recognize that the smoothing or low-pass filtering is an important process in the calculation of unforced multidecadal climate indices (Cane et al. 2017; Tung et al. 2019) and the effectiveness of slightly different smoothing on different indices has been studied (Frankcombe et al. 2018). However, compared to the discussion of detrending approaches, some influences caused by the low-pass filtering are relatively small, for example, the ordering of low-pass filtering and EOF analysis (Xu and Hu 2018), and as a result, the low-pass filtering is not detailed discussed in our study.

All indices are calculated from annual average temperatures (except for the ENSO), and standardized. The detrending approaches, which is critical in the calculations of all multidecadal indices, are discussed in detail in the next section.

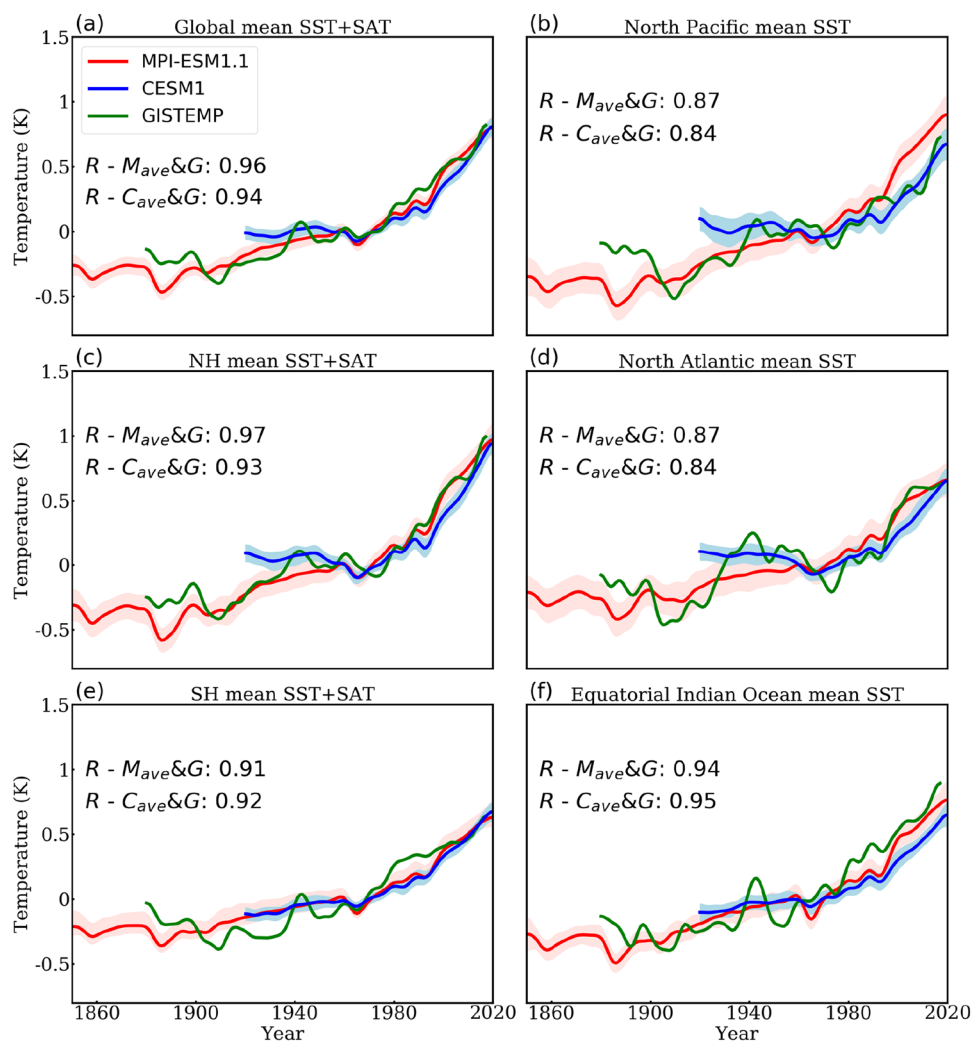
3 Separating the unforced climate variability from the forced climate response

Figure 1 shows the low-pass filtered surface temperature anomaly trends from 1850 to 2020 from the MPI-ESM1.1 and CESM1 ensembles, and from the GISTEMP. The long-term warming is apparent in both model results and the observation, whereas the warming rates among different regions are significantly different. Results from the GISTEMP show clear decadal variabilities, which are missed in the models due to the phase cancellations in the ensemble average. The temporal correlation coefficients between the ensemble-average MPI-ESM1.1 and GISTEMP are similar to those from the ensemble-average CESM1 and GISTEMP, and they (i.e., all of them are larger than 0.84) indicate that the two model ensembles both represent the positive temperature trends and the capability between MPI-ESM1.1 and CESM1 ensembles is generally similar to each other.

3.1 Comparison of various detrending approaches to isolate the internal variability

The temperature time series based on GISTEMP in Fig. 1 is a mixture of the forced signal (e.g., greenhouse gases, aerosols, solar radiation, volcanic eruptions and others) and

Fig. 1 Average surface temperature anomalies (sea surface temperature (SST) + surface air temperature (SAT)) relative to 1951–1980, smoothed by the 13-year low-pass filter for (a) global, (c) Northern Hemisphere, and (e) Southern Hemisphere, and regional average SST for (b) North Pacific, (d) North Atlantic, and (f) equatorial Indian Ocean. Red and blue lines are the means of 35 members from the CESM1 and 100 members from the MPI-ESM1.1 ensemble, respectively. Green lines represent the GISTEMP time series. The correlations between the averaged MPI-ESM1.1 results and GISTEMP ($R - M_{ave\&G}$), and correlations between the averaged CESM1 results and GISTEMP ($R - C_{ave\&G}$) are also given



unforced variability, whereas the time series based on MPI-ESM1.1 or CESM1 do not include the unforced variability due to the ensemble average. Thus, some studies used the difference between observation and ensemble-average time series to isolate the internal signals (Knight 2009; Terray 2012). However, how to obtain the unforced climate variability based on the simulation themselves is still in debate. Here we refer to this separation of forced and unforced temperature change as “detrending”. Some previous studies have investigated and evaluated various detrending approaches (Ting et al. 2009; Frankignoul et al. 2017), which are further examined here.

The performance of five different detrending approaches: global detrending (D1), regional detrending (D2), linear fit detrending (D3), quadratic fit detrending (D4), and local detrending via ensemble-average (D5), are evaluated in the rest of this Sect. 3.1.

The basic principle of global detrending approach (D1) is that the global-mean SST provides one of the most reasonable references to represent human-caused activities response,

and the anthropogenic forcing is assumed to be spatially uniform (Zhang et al. 1997). The forced component is assumed to be the global average (60°S – 60°N) SST time series, and it is then subtracted from each grid point of the ensemble member. Because the issue of the warming rates between different regions and globe does not receive much attention, the D1 approach is widely used in many studies (Trenberth and Shea 2006; Phillips et al. 2014). Proposed by Steinman et al. (2015), the D2 (i.e., regional detrending) approach is similar to the D1 approach, whereas the regional-average SST in the dominant region of corresponding unforced index [e.g., the regional average SST in the subpolar North Atlantic (40° – 60°N , 0° – 80°W) for AMO index, whereas for PDO, the dominant region is in the North Pacific Ocean (0° – 60°N , 110°E – 100°W)] is estimated as the response of SST to anthropogenic forcing, and it is subtracted in the detrending procedure.

For D1 and D2 in this study, the internal multidecadal climate indices are determined by: (1) calculating the mean temperature time series in the global- (D1 approach) or

region-coverage (D2 approach) for each model member, (2) estimating the forced signal by averaging the total members (e.g., 100 members for MPI-ESM1.1) temperature time series from step 1, (3) subtracting the forced component from each grid box to isolate the internal variability component, (4) performing the average or EOF-based analysis procedures over different dominant regions to obtain each internal multidecadal climate index for each member. We note that to avoid the influence of grid size differences, the latitude-weighted scheme is considered for both detrending and the indices compilation procedures for modes defined as the average of detrended SST.

The D3 (i.e., linear fit detrending) approach is one of the easiest choice that has been used by previous studies. It assumes the response to external forcing as a linear trend in time (Enfield et al. 2001). In this approach, the linear trend of temperatures at each grid point is subtracted from the original time series. The D4 (i.e., quadratic fit detrending) approach is similarly done at grid point, but assuming a high-order quadratic fit in the form as

$$Y = a + b \times t + c \times t^2$$

where Y is the quadratic fitted curve, t is the time, and the a , b , and c are coefficients. These two local detrending procedures do not require a (relatively) large ensemble and can be applied to observational record.

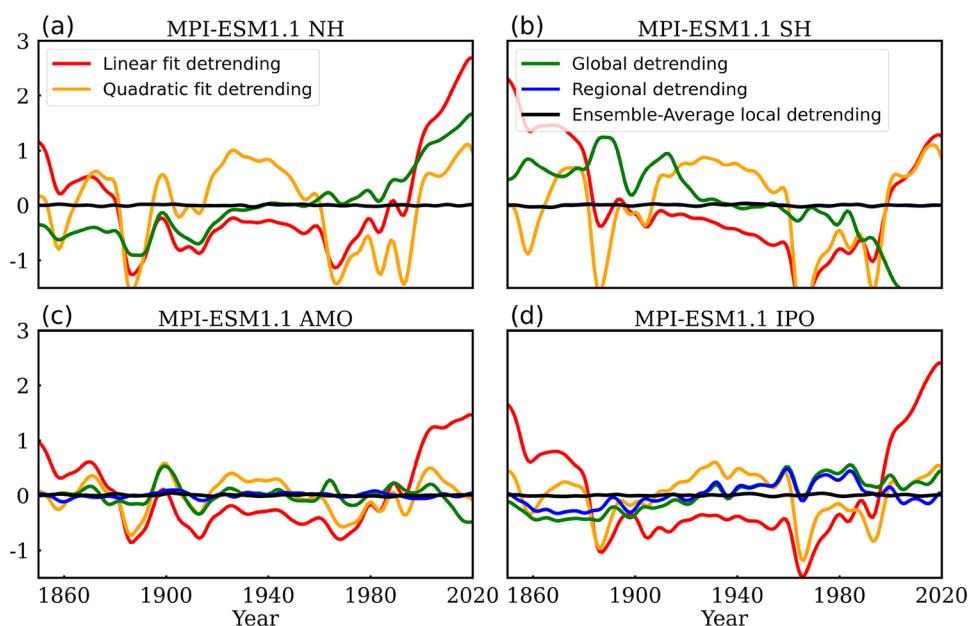
The D5 (i.e., local detrending via ensemble-average or ensemble-average local detrending) approach assumes that the ensemble average at each grid point is the forced component. The ensemble average is then subtracted from the time series of the corresponding grid point in each ensemble

member. However, this approach requires a sufficiently large ensemble size (of which we will discuss in depth in Sect. 3.2), so that the forced component can be robustly estimated as the ensemble average. Obviously, this approach is not applicable to observation.

Figure 2 compares the ensemble average of multidecadal variability using the five different detrending approaches. The ensemble average of climate indices estimated using the local linear fit detrending (red lines in Fig. 2) does a poor job. As argued by previous studies (Trenberth and Shea 2006; Bonfils and Santer 2011), this linear detrending approach fails to account for the nonlinearity of climate warming (such as the solar radiation, the acceleration due to faster greenhouse gas emission growth in the late twentieth century, and the unscheduled volcanic eruptions) and introduces large errors in both amplitude and phase of the estimated unforced variability (Frankcombe et al. 2015). Similar discrepancies, though to less extent, are also found in the quadratic fit detrending (orange lines in Fig. 2), which indicates that the quadratic fit detrending approach, although considering the nonlinearity of the time series, is still far from the optimal choice for removing the forced component.

The global detrending approach (green lines in Fig. 2) should address the nonlinear nature of climate change. This approach does remove much of the external forcing component, but some residual still remains, because the warming rates in the specific regions can be quite different from the global average. For example, the warming trend in the Northern Hemisphere in the twentieth century is known to be larger than the global mean trend. Thus, the global detrending procedure underestimates the role of external forcing in the NH, and some of the forced trend still

Fig. 2 Ensemble average of decadal variability of temperature in MPI-ESM1.1 simulation revealed by different detrending approaches: (a) NH, (b) SH, (c) AMO index (SAMO, TPI, and IOB are similar and not shown), and (d) IPO index (PDO and SPDO are similar and not shown)



contaminates the estimated unforced variability. Conversely, because of a slower regional warming, the externally forced signal is overestimated in the Southern Hemisphere, resulting in an artificial cooling in the unforced variability (green line in Fig. 2b), which should not have any long-term trend.

The ensemble average of unforced variability after the “regional detrending” approach is very closer to zero (blue lines in Fig. 2, but they are hard to be distinguished in Fig. 2a, b, c because the blue and black lines are very close to each other) compared with the results based on linear fit, quadratic fit, and global detrending approaches. However, the ensemble average of unforced modes in Fig. 2d still deviate from zero, because the warming evolution (as a function of time) for specific target region still fails to account for the spatial heterogeneity within the region. The residual signals are close to zero, only because the index is defined based on averaged detrended SST. The flaw is exacerbated when the EOFs are used in extracting the modes (such as the IPO in Fig. 2d). Thus, the regional detrending approach still cannot robustly isolate the unforced variability.

Finally, we show that the average of indices computed after the ensemble-average local detrending approach (black lines in Fig. 2) to be very close to zero. This clearly illustrates that these indices accurately capture unforced decadal variability. This makes the ensemble-average local detrending approach the preferred choice to isolate the unforced variability from the long-term climate record. We adopt this approach in the consequent analysis of this study.

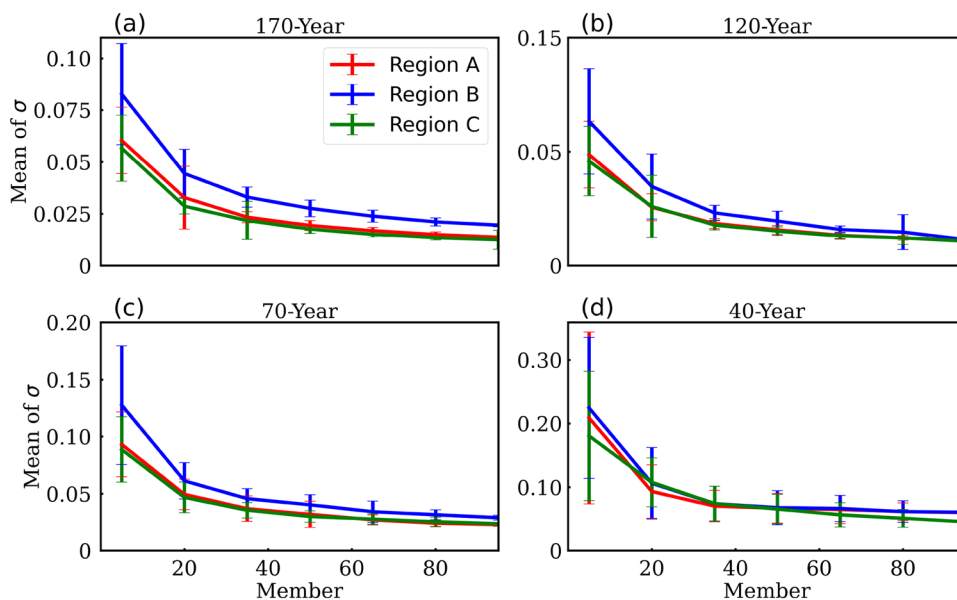
3.2 The ensemble size required to isolate the unforced variability

How big of an ensemble is required to effectively remove unforced variability? Frankignoul et al. (2017) evaluated various choices for removing the forced variability in climate models, and indicated that multidimensional ensemble empirical mode decomposition (EEMD) and the quadratic detrending approaches only remove the forced signals efficiently in one large ensemble model. Frankcombe et al. (2018) also suggested that the ensemble average from a single ensemble model is a good option for the estimation of the forced component, even with few ensemble members.

We take advantage of the size of the MPI-ESM1.1 grand ensemble to investigate the question. We generate synthetic sub-ensembles by randomly selecting members of the MPI-ESM1.1 ensemble. For each potential ensemble size, we produce 100 random sub-ensembles. As we mentioned before, if the forced component is removed from the temperature trends perfectly, the ensemble averaged time series is expected to be close to zero when the ensemble size is large enough. The root mean square error (RMSE) of the average unforced temperature time series (such as the visible deviation of colored lines from zero in Fig. 2) can therefore be used as a metric to evaluate how well the forced response is removed. Figure 3 shows the RMSE of each sub-ensemble size, and the bars indicate the uncertainties (calculated as the standard deviation) of that size.

The RMSEs rapidly decrease as the number of ensemble members increases from 5 to 35. For larger time scales (e.g., 170-year in Fig. 3a: trend since 1850 or 120-year in Fig. 3b: trend since 1900), as the size increase approximately to more than 50, the errors become close to those

Fig. 3 The root mean square error (σ) as a function of the size of sub-ensembles for different time scales (**a**: 170-year, **b**: 140-year, **c**: 70-year, and **d**: 40-year) and different spatial scales (Region A: 60°S–60° N, 110°E–70°W, Region B: 0°–60° N, 110°E–100°W, and Region C: 30°S–30°N, 40°E–120°E). The error bars indicate the uncertainties (standard deviation) derived from 100 sub-ensembles and the sub-ensembles are generated by randomly sampling from the 100-member MPI-ESM1.1 ensemble



from the grand ensemble with 100 members. It means that adding more ensemble members products little benefit. The result suggests that the forced component can be robustly removed from the climate record and thus an ensemble of ~ 50 members can isolate the unforced variability at centennial scale (Fig. 3a, b). However, if the time scale is shorted to 70-year (Fig. 3c: trend since 1950) or 40-year (Fig. 3d: trend since 1980), the RMESs are significantly larger, and more ensemble members (approximately 65 or larger) are needed. To further investigate potential relationship between the optimal ensemble size and different spatial coverages, we perform the comparison among three typical regions, i.e., Region A: 60°S – 60°N , 110°E – 70°W , Region B: 0° – 60°N , 110°E – 100°W , and Region C: 30°S – 30°N , 40°E – 120°E . With the decrease of the Regions A, B, and C areas, the RMSEs and optimal ensemble size do not increase proportionally. The evolutions over ensemble members for Region C are similar to those for Region A, suggesting that the optimal size to effectively isolate the internal signal is more related to region characteristic than the spatial scale. We notice only one ensemble model (i.e., MPI-ESM1.1) is analyzed in this study, and the requirement for number of ensemble member may slightly differ for different ensemble models.

3.3 Characteristics of climate indices and the lead-lag relationships of Atlantic and Pacific decadal variability

First of all, we analyze various climate indices based on ensemble-average local detrending approach of the full MPI-ESM1.1 (100 members) and CESM1 (35 members) ensembles.

The correlation patterns between the unforced climate modes and the global surface temperature are shown in Fig. 4. Also shown are the spatial patterns based on the results from GISTEMP using a quadratic fit detrending. The correlation pattern of the PDO is characterized by two negative centers in the central-western regions of the north and south subtropical Pacific, and a large positive feature in the central-eastern tropical Pacific. Both negative centers of the PDO pattern are well captured in the MPI-ESM1.1 and CESM1 as in the GISTEMP observations.

However, large differences are seen in the AMO patterns. The MPI-ESM1.1's and CESM1's AMO correlation patterns are characterized as a horseshoe-like field in the North Atlantic, whereas the feature is significantly strong and with less variation in the GISTEMP pattern. Correlations are also much further away from the North Atlantic in the observations. The features are also shown for patterns of the IOB. This should be attribute to the imperfect detrending approach used in the observed dataset. As discussed before, the quadratic fit detrending approach used for GISTEMP is not as

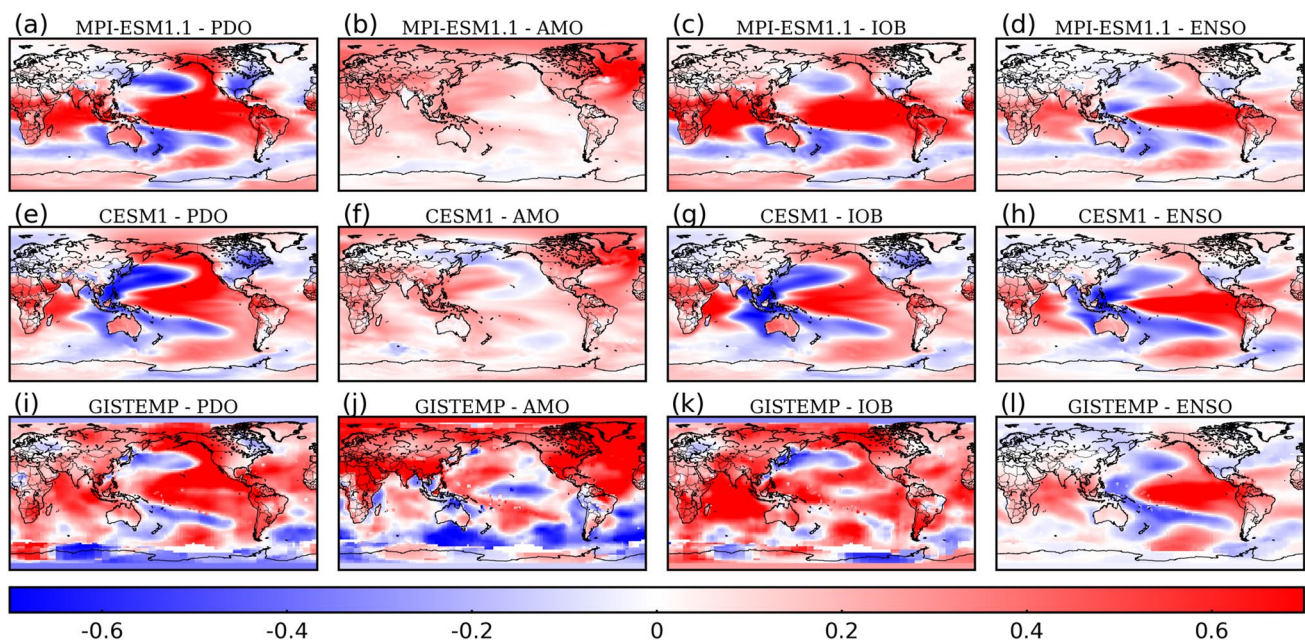


Fig. 4 The spatial pattern of correlation coefficient between surface temperature and different indices during 1920–2017 of the MPI-ESM1.1 ensemble, the CESM1 ensemble, and GISTEMP. For the ensembles, the value plotted is the average of the correlation fields

from all individual ensemble members. Note the unforced climate indices for MPI-ESM1.1 and CESM1 are based on the ensemble-average local detrending approach, whereas the indices for GISTEMP are based on the local quadratic fit detrending approach

good as the ensemble-average local detrending approach and an effective approach to isolate unforced variability from a single member record still needs to be improved. This could cause higher correlation coefficients between the AMO/IOB (and less so for the PDO) and global temperature fields (as shown in Fig. 4j, k), because the forced response is not completely removed from the climate record.

To further estimate the temporal characteristics of different modes in the Atlantic and Pacific, Fig. 5 shows the frequency distribution of the period of all members for indices from MPI-ESM1.1 and CESM1. It is indicated from the results that the dominant period of the PDO is around 30–60 years. More than half members in both MPI-ESM1.1 and CESM1 confirm a 30–50-year period of the IOB. However, 46% and 40% members in MPI-ESM1.1 and CESM1 models have similar autocorrelation characteristics (not shown here) reflect the dominant period is ~50 to 70-year for the AMO. Significant period distribution peaks in 50–60- and 35–45-year bands for the NH and SH, respectively, suggest a larger cycle period of the NH mode. This feature further indicates that the unforced climate variability in the North Atlantic might have dominated the Northern Hemisphere's climate variability in a similar long-term decadal time scale.

Now, we investigate the correlation between different climate indices with various lead-lag times. For effectively demonstrating the results, another ensemble model, CanESM2 (the second-generation version of the Canadian Earth System Model, Flato et al. 2000) with 50 members, is considered. It is clear that the PDO, IPO, and SPDO are highly correlated, and the time evolution of the three indices is similar. The ensemble average peak correlations between the IPO and PDO (Fig. 6a) and between the PDO and SPDO (Fig. 6c) in MPI-ESM1.1 indices are 0.93 and 0.81,

respectively. Similar lead-lag characteristics are also found in the results from CESM1 and CanESM2 ensembles (blue and green lines in Fig. 6, respectively).

The relationship between the decadal climate variability in the North Pacific and North Atlantic has been extensively studied and reviewed (Zhang et al. 2019). For example, Zhang and Delworth (2007) compared the simulated and observed SST in the Pacific and Atlantic, and they found that the AMO contributed to the PDO. Their study indicated that the simulated unfiltered AMO leads the simulated PDO by 3 years with a maximum correlation of 0.66, and the observed unfiltered AMO leads the PDO by 12 years with a maximum correlation of 0.47. Other studies also suggested a strong relationship between the AMO and PDO. d'Orgeville and Peltier (2007) used SST dataset from Hadley Center (Rayner et al. 2003) to show that the AMO leads PDO by 13 years or lags PDO by 17 years. This is further supported by Li and Luo (2013), who suggested that the PDO leads the AMO by 19–21 years, with a 0.71 correlation coefficient, or the AMO leads PDO by 16–18 years with a coefficient of 0.84. Furthermore, Wu et al. (2011) showed that the AMO lead PDO by 11–12 years, but the correlation coefficient is a more modest 0.35.

However, based on our analysis in Fig. 6b, a small (less than 0.2) correlation coefficient showing the PDO leading AMO by 3 to 10 years is found in the ensembles, suggesting that the lead-lag relationship between the simulated AMO and PDO in these ensembles is not in agreement with previous observation-based studies. Our analysis uses the most-effective detrending approach, the ensemble-average local detrending approach, which requires a large ensemble to perform. Similar to the discussion of indices compiled by MPI-ESM1.1 model, analysis based on some other large ensemble models (e.g., the 35-member CESM1 and 50-member

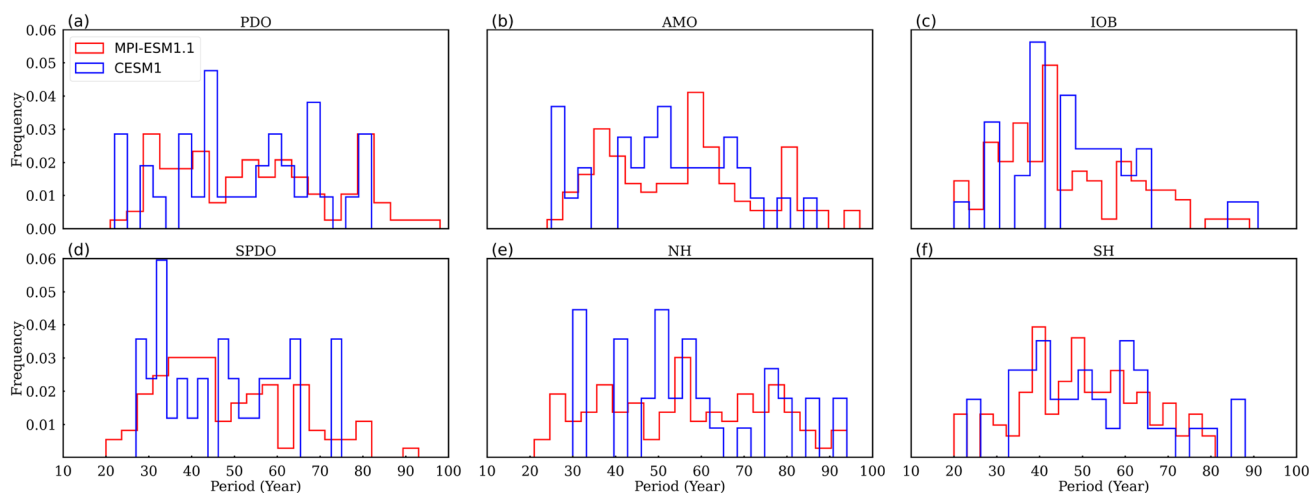
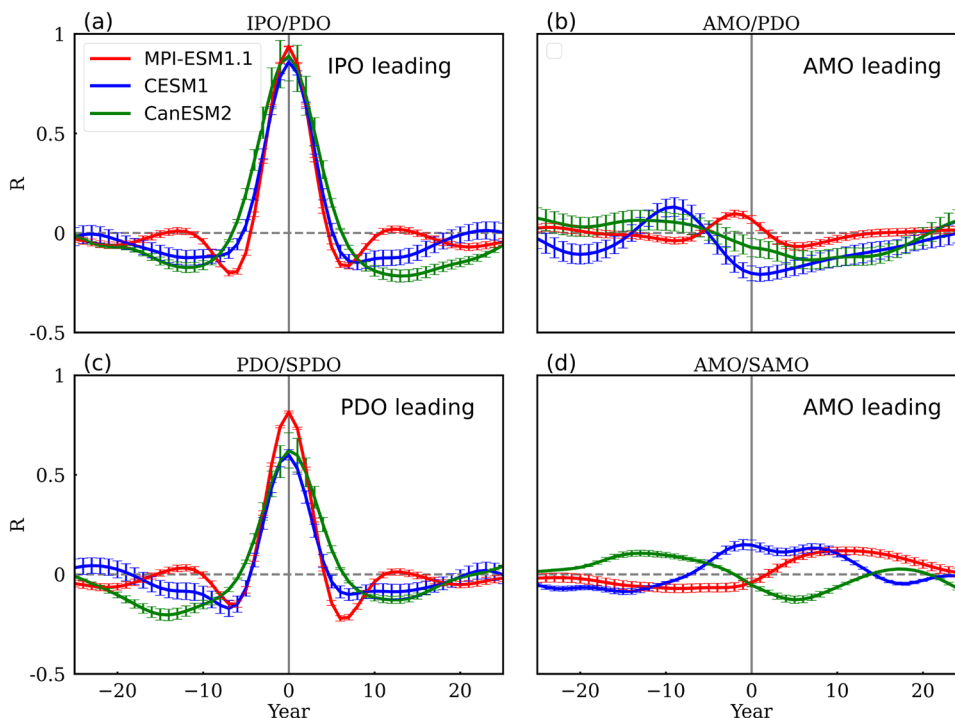


Fig. 5 Frequency distribution of different unforced climate indices from all members. The red and blue boxes indicate the results based on MPI-ESM1.1 and CESM1 ensembles, respectively

Fig. 6 Cross (lead-lag) correlations between (a) IPO and PDO, (b) AMO and PDO, (c) PDO and SPDO, and (d) AMO and SAMO. The results are the average correlation coefficients of the individual ensemble member, and the error bars are the standard deviations scaled by $1/\sqrt{N}$, with N being the number of ensemble members ($N=100$ for MPI-ESM1.1, $N=35$ for CESM1, and $N=50$ for CanESM2)



CanESM2 ensemble models) together indicate that there is no significant correlation between the AMO and PDO.

Moreover, as a test, we isolate the unforced signal in the ensemble model by using other flawed detrending approaches, and surprisingly high correlations in the lead-lag relationship are found. For example, the maximum correlation coefficients are 0.78 and 0.42 (red and blue lines in Fig. 7a) showing the AMO leading PDO, if using “linear fit detrending” and “quadratic fit detrending” in MPI-ESM1.1 ensemble model, respectively. Although the maximum coefficients from the quadratic fit detrending based results in CESM1 and CanESM2 models are not as large as those in MPI-ESM1.1, the peak values of 0.65 and 0.92 from the linear fit detrending based results in CESM1 and CanESM2 further demonstrate that the imperfect detrending approach

should be the cause of high linkages between the AMO and PDO modes. This is agreement with the study of Steinman et al. (2015), who argued that statistically significant correlation between the two indices suggested by previous studies may be due to biases in the linear detrending approach (which is more severe than quadratic detrending in Fig. 7). Moreover, we also find that the low-pass filter at different frequencies will not significantly influence the relationship between the PDO and AMO (not shown here). Lastly, we note that the PDO and AMO relationship inferred from the models can shed insights on the uncertainty of the previous analysis, but we cannot conclusively claim that model-inferred relationship indeed is what happened in the real world, which has provided limited sampling (during modern era) from tackling AMO-PDO interaction.

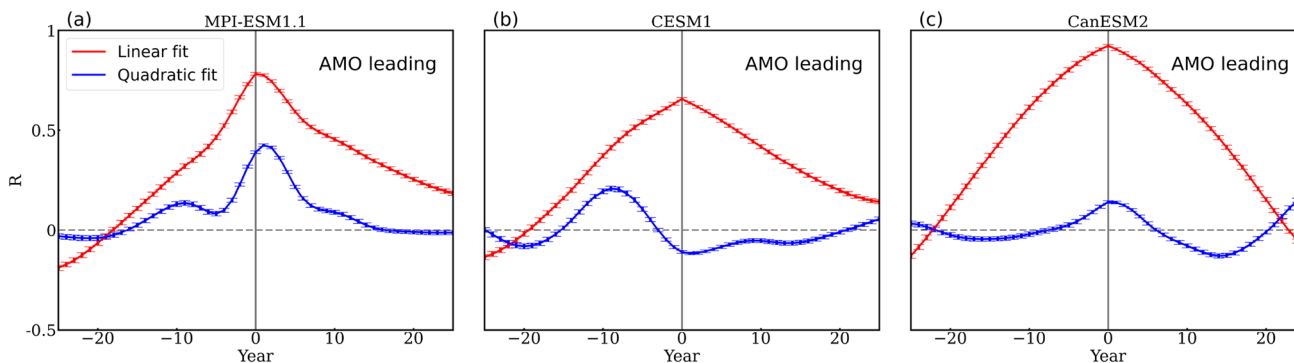


Fig. 7 Same as Fig. 6 but based on linear fit detrending and quadratic fit detrending in (a) MPI-ESM1.1, (b) CESM1, and (c) CanESM2

4 Summary

We have calculated indices for a suite of well-known modes of unforced variability (i.e., PDO, SPDO, IPO, TPI, AMO, SAMO, IOB, and ENSO) in two large ensembles of climate model runs: a 100-member ensemble of the Max Planck Institute Earth System Model (MPI-ESM1.1) and a 35-member ensemble of CESM1. We have made the compiled indices publicly available for other researchers to use in their analyses.

Decomposing the forced response and the unforced variability in climate records is a key procedure in obtaining accurate multidecadal climate modes. We examine five different approaches for removing the forced component from the temperature time series. It is found that most of the techniques, despite widely used in previous studies, do a poor job to isolate the unforced variations in the model output. The best estimates came from the ensemble-average local detrending approach, in which the ensemble average time series at each grid point is subtracted from the time series of each individual ensemble member. However, note that it is still difficult of isolating the unforced variability from a single ensemble member effectively. We also suggest that approximately 50 members are required in an ensemble to isolate the unforced variability cleanly at a centennial scale, and more ensemble members are needed for shorter time scale (e.g., years from the satellite record). Meanwhile, more future studies are needed to further investigate the relationship between optimal ensemble size and different regions.

Most importantly, low correlation coefficients between the AMO and PDO in the two large ensembles indicate that there is no statistically robust linkage between climate variability in the Pacific and Atlantic in the two ensembles (Steinman et al., 2015). This challenges some previous studies (Zhang and Delworth 2007; d'Orgeville and Peltier 2007; Wu et al. 2011; Li and Luo 2013), which were problematic due to the inevitable issue of removing the forced component from the surface temperature data suggested by our work. A further examination of this plausible Pacific-Atlantic linkage is motivated by the recent CLIVAR (Climate Variability and Predictability Program) effort of producing a diverse group of large ensembles by various modeling centers. Possible research efforts also include taking advantage of the long-term pre-industrial control simulation of CMIP6 models, and the emerging paleoclimate reanalysis of the last Millennium.

Acknowledgements We acknowledge funding support by the Natural Science Foundation of Jiangsu Province (BK20190093) and the Young Elite Scientists Sponsorship Program of CAST (2017QNRC001). Xu and Dessler acknowledge funding from the US National Science Foundation Climate and Large-scale Dynamics Program (AGS-1841308).

Data availability Calculated climate indices as well as the code used to process the model output can be found at https://github.com/carolyb/climate_index. MPI-ESM1.1 ensemble model code can be downloaded from <https://mpimet.mpg.de/en/science/modeling-with-icon/code-availability>, and the datasets from MPI-ESM are available from <https://esgf-node.llnl.gov/search/cmip6/>. The CESM1 data can be found from <https://www.cesm.ucar.edu/projects/community-projects/LENS/datasets.html>, and the CanESM2 data can be downloaded from <http://crd-data-donnees-rdc.ec.gc.ca/CCCMA/products/CanSISE/output/CCCma/CanESM2>.

Declarations

Conflict of interest The authors declare that they have no conflict of interest.

References

- Bonfils C, Santer BD (2011) Investigation the possibility of a human component in various Pacific decadal oscillation indices. *Clim Dyn* 37:1457–1468. <https://doi.org/10.1007/s00382-010-0920-1>
- Cai W, Wu L, Legaigne M et al (2019) Pantropical climate interactions. *Science* 363:944. <https://doi.org/10.1126/science.aav4236>
- Cane MA, Clement AC, Murphy LN, Bellomo K (2017) Low-pass filtering, heat flux, and atlantic multidecadal variability. *J Clim* 30:7259–7553. <https://doi.org/10.1175/JCLI-D-16-0810.1>
- Chiang JCH, Lintner BR (2005) Mechanisms of remote tropical surface warming during El Niño. *J Clim* 15:2616–2631
- Clement A, Bellomo K, Murphy LN, Cane MA, Mauritsen T, Radal G, Stevens B (2015) The Atlantic multidecadal oscillation without a role for ocean circulation. *Science* 350:320–324. <https://doi.org/10.1126/science.aab3980>
- Dai A (2013) The influence of the inter-decadal Pacific oscillation on US precipitation during 1923–2010. *Clim Dyn* 41:633–646. <https://doi.org/10.1007/s00382-012-1446-5>
- Delworth TL, Zhang R, Mann ME (2007) Decadal to centennial variability of the Atlantic from observations and models. *Ocean Circulation: Mechanisms and Impacts*, Geophysical Monograph Series 173, Washington, DC, American Geophysical Union, pp 131–148
- Deser C, Phillips AS, Bourdette V, Teng HY (2012) Uncertainty in climate change projections: the role of internal variability. *Clim Dyn* 38:527–546. <https://doi.org/10.1007/s00382-010-09770-x>
- Dong L, McPhaden MJ (2017a) Why has the relationship between Indian and Pacific Ocean decadal variability changed in recent decades? *J Climate* 30:1971–1983. <https://doi.org/10.1175/JCLI-D-16-0313.1>
- Dong L, McPhaden MJ (2017b) The role of external forcing in the internal variability in regulating global mean surface temperatures on decadal timescales. *Environ Res Lett* 12:034011. <https://doi.org/10.1088/1748-9326/aa5dd8>
- Dong L, Zhou T, Dai A, Song F, Wu B, Chen X (2016) The footprint of the Inter-decadal Pacific Oscillation in Indian Ocean sea surface temperatures. *Sci Rep* 6:21251. <https://doi.org/10.1038/srep21251>
- Dong L, Leung LR, Lu J, Song F (2021) Double-ITCZ as an emergent constraint for future precipitation over Mediterranean climate regions in the North Hemisphere. *Geophys Res Lett* 48:e2020GL091569. <https://doi.org/10.1029/2020GL091569>
- d'Orgeville M, Peltier WR (2007) On the pacific decadal oscillation and the atlantic multidecadal oscillation: might they be related? *Geophys Res Lett* 34:L23705. <https://doi.org/10.1029/2007GL031584>

- Enfield DB, Mestas-Nuñez AM, Trimble PJ (2001) The Atlantic multi-decadal oscillation and its relation to rainfall and river flows in the continental U.S. *Geophys Res Lett* 28:2077–2080. <https://doi.org/10.1029/2000GL012745>
- England MH, McGregor S, Spence P, Meehl GA, Timmermann A, Cai W, Gupta AS, McPhaden MJ, Purich A, Santoso A (2014) Recent intensification of wind-driven circulation in the Pacific and the ongoing warming hiatus. *Nat Climate Change* 4:222–227. <https://doi.org/10.1038/nclimate2106>
- Flato GM, Boer GJ, Lee WG, McFarlane NA, Ramsden D, Reader MC, Weaver AJ (2000) The Canadian centre for climate modeling and analysis global coupled model and its climate. *Climate Dyn* 16:451–467. <https://doi.org/10.1007/s003820050339>
- Frankcombe LM, England MH, Mann ME, Steinman BA (2015) Separating internal variability from the externally forced climate response. *J Clim* 28:8184–8202. <https://doi.org/10.1175/JCLI-D-15-0069.1>
- Frankcombe LM, England MH, Kajtar JB, Mann ME, Steinman BA (2018) On the choice of ensemble mean for estimating the forced signal in the presence of internal variability. *J Clim* 31:5681–5693. <https://doi.org/10.1175/JCLI-D-17-0662.1>
- Frankignoul C, Hasselmann K (1977) Stochastic climate models, part II: application to sea-surface temperature variability and thermocline variability. *Tellus* 29:289–305. <https://doi.org/10.3402/tellusa.v29i4.11362>
- Frankignoul C, Gastineau G, Kwou YO (2017) Estimation of the SST response to anthropogenic and external forcing and its impact on the atlantic multidecadal oscillation and the pacific decadal oscillation. *J Clim* 30:9871–9895. <https://doi.org/10.1175/JCLI-D-17-0009.1>
- Henley BJ, Gergis J, Karoly DJ, Power S, Kennedy J, Folland CK (2015) A tripole index for the interdecadal pacific oscillation. *Clim Dyn* 45:3077–3090. <https://doi.org/10.1007/s00382-015-2525-1>
- Huang D, Dai A, Yang B, Yan P, Zhu J, Zhang Y (2019) Contributions of different combinations of the IPO and AMO to recent changes in winter East Asian jets. *J Clim* 32:1607–1626. <https://doi.org/10.1175/JCLI-D-18-0218.1>
- Hurrell JW, Holland MM, Gent PR et al (2013) The community earth system model: a framework for collaborative research. *Bull Amer Meteor Soc* 94:1339–1360. <https://doi.org/10.1175/BAMS-D-12-00121.1>
- Kay JE, Deser C, Phillips A et al (2015) The community earth system model (CESM) large ensemble project: a community resource for studying climate change in the presence of internal climate variability. *Bull Amer Meteor Soc* 96:1333–1349. <https://doi.org/10.1175/BAMS-D-13-00255.1>
- Kerr RA (2000) A north atlantic climate pacemaker for the centuries. *Science* 288:1984–1985. <https://doi.org/10.1126/science.288.5473.1984>
- Kim WM, Yeager S, Chang P, Danabasoglu G (2018) Low frequency North Atlantic climate variability in the community earth system model large ensemble. *J Clim* 31:787–813
- Klein SA, Soden BJ, Lau NC (1999) Remote sea surface temperature variations during ENSO: evidence for a tropical atmospheric bridge. *J Climate* 106:4681–4693
- Knight JR (2009) The Atlantic multidecadal oscillation inferred from the forced climate response in coupled general circulation models. *J Clim* 22:1610–1625. <https://doi.org/10.1175/2008JCLI2628.1>
- Knight JR, Allan RJ, Folland CK, Vellinga M, Mann ME (2005) A signature of persistent natural thermohaline circulation cycles in observed climate. *Geophys Res Lett* 32:L20708. <https://doi.org/10.1029/2005GL024233>
- Lenssen N, Schmidt G, Hansen J, Mennu M, Persin A, Ruedy R, Zys D (2019) Improvements in the GISTEMP uncertainty model. *J Geophys Res* 124:6307–6326. <https://doi.org/10.1029/2018JD029522>
- Levine AFZ, McPhaden MJ, Frierson DMW (2017) The impact of the AMO on multidecadal ENSO variability. *Geophys Res Lett* 44:3877–3886. <https://doi.org/10.1002/2017GL072524>
- Li S, Luo F (2013) Lead-lag connection of the atlantic multidecadal oscillation (AMO) with East Asian surface air temperatures in instrumental records. *Atmos Oceanic Sci Lett* 6:138–143
- Lu R, Dong B, Ding H (2006) Impact of the Atlantic multidecadal oscillation on the Asian summer monsoon. *Geophys Res Lett* 33:L24701. <https://doi.org/10.1029/2006GL027655>
- Maher N, Milinski S, Suarez-Gutierrez L (2019) The max planck institute grand ensemble: enabling the exploration of climate system variability. *J Adv Model Earth Syst* 11:2050–2069. <https://doi.org/10.1029/2019MS001639>
- Mantua NJ, Hare SR (2002) The Pacific Decadal Oscillation *J Oceanogr* 58:35–44. <https://doi.org/10.1023/A:1015820616384>
- Mantua NJ, Hare SR, Zhang Y, Wallace JM, Francis RC (1997) A pacific interdecadal climate oscillation with impacts on salmon production. *Bull Amer Meteorol Soc* 78:1069–1079. [https://doi.org/10.1175/1520-0477\(1997\)078%3c1069:APICOW%3e2.0.CO;2](https://doi.org/10.1175/1520-0477(1997)078%3c1069:APICOW%3e2.0.CO;2)
- McGregor S, Timmermann A, Stuecker MF, England MH, Merrifield M, Jin F, Chikamoto Y (2014) Recent walker circulation strengthening and pacific cooling amplified by atlantic warming. *Nat Climate Change* 4:888–892. <https://doi.org/10.1038/NCLIMATE2330>
- Meehl GA, Washington WM, Arblaster JM et al (2013) Climate change projections in CESM1(CAM5) compared to CCSM4. *J Clim* 26:6287–6308. <https://doi.org/10.1175/JCLI-D-12-00572.1>
- Meehl GA, Arblaster JM, Bitz CM, Chung CTY, Teng H (2016) Antarctic sea-ice expansion between 2000 and 2014 driven by tropical Pacific decadal climate variability. *Nat Geosci* 9:590–595. <https://doi.org/10.1038/ngeo2751>
- Micevski T, Franks SW, Kuczera G (2006) Multidecadal variability in coastal eastern Australian flood data. *J Hydrol* 327:219–225. <https://doi.org/10.1016/j.jhydrol.2005.11.017>
- Newman M, Alexander MA, Ault TR et al (2016) The pacific decadal oscillation, revisited. *J Clim* 29:4399–4427. <https://doi.org/10.1175/JCLI-D-15-0508.1>
- O'Reilly CH, Huber M, Woollings T, Zanna L (2016) The signature of low-frequency oceanic forcing in the Atlantic multidecadal oscillation. *Geophys Res Lett* 43:2810–2818
- Phillips AS, Deser C, Fasullo J (2014) Evaluating modes of variability in climate models. *Eos Trans Amer Geophys Union* 95:453–455. <https://doi.org/10.1002/2014EO490002>
- Power S, Casey T, Folland C, Colman A, Mehta V (1999) Inter-decadal modulation of the impact of ENSO on Australia. *Clim Dyn* 15:319–324. <https://doi.org/10.1007/s003820050284>
- Qian C, Zhou T (2014) Multidecadal variability of North China aridity an20d its relationship to PDO during 1900–2010. *J Clim* 27:1210–1222. <https://doi.org/10.1175/JCLI-D-13-00235.1>
- Rayner NA, Parker DE, Horton EB, Folland CK, Alexander LV, Rowell DP, Kent EC, Kaplan A (2003) Global analyses of sea surface temperature, sea ice, and night marine air temperature since the late nineteenth century. *J Geophys Res* 108:4407. <https://doi.org/10.1029/2002JD002670>
- Schlesinger M, Ramankutty N (1994) An Oscillation in the global climate system of period 65–70 years. *Nature* 367:723–726. <https://doi.org/10.1038/367723a0>
- Si D, Ding Y (2016) Oceanic forcings of the interdecadal variability in east asian summer rainfall. *J Clim* 29:7633–7649. <https://doi.org/10.1175/JCLI-D-15-0792.1>
- Si D, Hu A (2017) Internally generated and externally forced multidecadal oceanic modes and their influence on the summer rainfall

- over East Asia. *J Clim* 30:8299–8316. <https://doi.org/10.1175/JCLI-D-17-0065.1>
- Song F, Zhou T (2014a) Interannual variability of East Asian summer monsoon simulated by CMIP3 and CMIP5 AGCMs: Skill Dependence On Indian Ocean-Western Pacific Anticyclone Teleconnection. *J Clim* 27:1679–1697. <https://doi.org/10.1175/JCLI-D-132-00248.1>
- Song F, Zhou T (2014b) The climatology and interannual variability of East Asian summer monsoon in CMIP5 coupled models: Does air-sea coupling improve the simulations? *J Clim* 27:8761–8777
- Song F, Zhou T (2015) The dominant role of internal variability in modulating the decadal variation of the East Asian summer monsoon-ENSO relationship during the 20th century. *J Clim* 28:7093–7107
- Song F, Zhou T, Qian Y (2014) Responses of East Asia summer monsoon to natural and anthropogenic forcings in the 17 latest CMIP5 models. *Geophys Res Lett* 41:596–603
- Steinman BA, Mann ME, Miller SK (2015) Atlantic and Pacific multidecadal oscillations and Northern Hemisphere temperatures. *Science* 347:988–991. <https://doi.org/10.1126/science.1257856>
- Terry L (2012) Evidence for multiple drivers of North Atlantic multidecadal climate variability. *Geophys Res Lett* 39:L19712. <https://doi.org/10.1029/2012GL053046>
- Ting M, Kushnir Y, Seager R, Li C (2009) Forced and Internal Twentieth-Century SST Trends in the North Atlantic. *J Clim* 22:1469–1481. <https://doi.org/10.1175/2008JCLI2561.1>
- Trenberth KE, Shea DJ (2006) Atlantic hurricanes and natural variability in 2005. *Geophys Res Lett* 33:L12704. <https://doi.org/10.1029/2006GL026894>
- Trenberth KE, Jones PD, Ambenje P et al (2007) Observations: surface and atmospheric climate change, climate change 2007: the physical science basis. Cambridge University Press, Cambridge New York, pp 237–336
- Tung K, Chen X, Zhou J, Li K (2019) Interdecadal variability in pan-Pacific and global SST, revisited. *Clim Dyn* 52:2145–2157. <https://doi.org/10.1007/s00382-018-4240-1>
- Wild M, Folini D, Schär C, Loeb N, Dutton EG, König-Langlo K (2013) The global energy balance from a surface perspective. *Clim Dyn* 40:3107–3134. <https://doi.org/10.1007/s00382-012-1569-9>
- Wu S, Liu Z, Zhang R, Delworth TL (2011) On the observed relationship between the Pacific decadal oscillation and the atlantic multi-decadal oscillation. *J Oceanogr* 67:27–35. <https://doi.org/10.1007/s10872-011-0003-x>
- Xie SP, Du Y, Huang G, Zheng XT, Tolinaga H, Hu K, Liu Q (2010) Decadal shift in EI Niño influences on Indo-western Pacific and East Asian climate in the 1970s. *J Climate* 23:3352–3368
- Xu Y, Hu A (2018) How would the twenty-first-century warming influence pacific decadal variability and its connection to north american rainfall: assessment based on a revised procedure for the IPO/PDO. *J Clim* 31:1547–1563. <https://doi.org/10.1175/JCLI-D-17-0319.1>
- Yang J, Liu Q, Xie SP, Liu Z, Wu L (2007) Impact of the Indian Ocean SST basin mode on the Asian summer monsoon. *Geophys Res Lett* 34:L02708. <https://doi.org/10.1029/2006GL028571>
- Zhang R (2017) On the persistence and coherence of subpolar sea surface temperature and salinity anomalies associated with the Atlantic multidecadal variability. *Geophys Res Lett* 44:7865–7875. <https://doi.org/10.1002/2017GL074342>
- Zhang R, Delworth TL (2006) Impact of Atlantic multidecadal oscillations on Indian/Sahel rainfall and Atlantic hurricanes. *Geophys Res Lett* 33:L17712. <https://doi.org/10.1029/2006/GL026267>
- Zhang R, Delworth TL (2007) Impact of the Atlantic Multidecadal Oscillation on North Pacific climate variability. *Geophys Res Lett* 34:L23708. <https://doi.org/10.1029/2007GL031601>
- Zhang Y, Wallace JM, Battisti DS (1997) ENSO-like Interdecadal Variability: 1900–93. *J Clim* 10:1004–1020. [https://doi.org/10.1175/1520-0422\(1997\)010%3c1004:ELIV%3e2.0.CO;2](https://doi.org/10.1175/1520-0422(1997)010%3c1004:ELIV%3e2.0.CO;2)
- Zhang R, Sutton R, Danabasoglu G, Kwon Y, Marsh R, Yeager SG, Amrhein DE, Little CM (2019) A review of the role of the atlantic meridional overturning circulation in atlantic multidecadal variability and associated climate impacts. *Rev Geophys* 57:316–375. <https://doi.org/10.1029/2019RG000644>
- Zhou T, Song F, Lin R, Chen X, Chen X (2013) The 2012 North China floods: explaining an extreme rainfall event in the context of a long-term drying tendency [in “explaining extreme event of 2012 from a climate perspective”]. *Bull Amer Meteor Soc* 94:S49–S51

Publisher's Note Springer Nature remains neutral with regard to jurisdictional claims in published maps and institutional affiliations.